J. Fluid Mech. (1984), *vol.* 149, *pp.* 179–203
Printed in Great Britain

Experimental determination of the three-dimensional vorticity field in the boundary-layer transition process

By D. R. WILLIAMS†, H. FASEL‡ AND F. R. HAMA‖
Princeton University, New Jersey

(Received 25 August 1983 and in revised form 13 June 1984)

The vortex loop observed in flow-visualization studies of boundary-layer transition has been investigated by mapping the instantaneous velocity and vorticity fields. All three velocity components have been measured with hot-film anemometers at numerous grid points in a measuring volume centred on the location where the vortex loop appears in flow-visualizaton studies. The instantaneous vorticity field has been computed from the velocity field, and the vortex loop is revealed in the longitudinal component of vorticity. The loop propagates downstream at approximately the primary disturbance wavespeed. The fluid in the outer part of the boundary layer travels faster, and flows over the loop. This forms the inflexional high-shear layer, which breaks down into the hairpin vortices. The magnitude of the vorticity in the high-shear layer is actually about three times larger than that in the loop. These two regions of vorticity are distinguished by the direction of the instantaneous vorticity vectors, i.e. the vectors in the high-shear layer run in the spanwise direction, while the vectors in the vortex loop run primarily in the downstream direction. This also explains why the loop cannot be detected with simple $\partial u/\partial y$ measurements.

1. Introduction

Transition from laminar to turbulent flow in a flat-plate boundary layer has been intensively studied since the classical work of Schubauer & Skramstad (1948), in which they were able to verify experimentally the linear stability theory of Tollmien (1931, 1936) and Schlichting (1933, 1935). It was recognized, however, that the larger part of the transition process involved highly nonlinear and, moreover, three-dimensional developments before the boundary layer actually became turbulent. Many elaborate experimental and theoretical investigations have attempted to clarify the later stages of transition; however, no comprehensive theory exists which can explain them, on the one hand, and there is no general agreement on the exact physical processes involved, on the other.

The apparently simple mean-flow geometry of the Blasius boundary layer on a flat plate must undergo a complicated set of manoeuvres to become turbulent. The current understanding of transition can be summarized in a list of ten stages:

I, appearance of two-dimensional small-amplitude linear oscillations (Tollmien–Schlichting waves);

† Present address: Illinois Institute of Technology, Chicago.
‡ Present address: University of Arizona, Tucson.
‖ Present address: Stuttgart University, Stuttgart, West Germany.

II, amplification (or damping) of TS waves;
III, large-amplitude nonlinear oscillations;
IV, emergence of transversely periodic three-dimensionality;
V, formation of longitudinal vortices and their intensification;
VI, formation of inflexional high-shear layer;
VII, appearance of multiple hairpin eddies (spikes);
VIII, local breakdown (initial appearance of random motions);
IX, formation of a turbulent spot;
X, coagulation of turbulent spots (turbulent flows).

The first two steps are well described by the linear stability theory. When the disturbance amplitude of the streamwise velocity component exceeds about $0.01U_0$, where U_0 is the free-stream velocity, certain nonlinear effects appear in its amplification characteristics (step III). The true fluid-dynamic nature of the nonlinear waves, however, is not yet quite accurately described. In spite of some recent theoretical attempts, it is still not known how the three-dimensionality of the disturbance originated or which parameters influence it (step IV). The formation of the longitudinal component of vorticity and, subsequently, the inflexional high-shear layer (steps V and VI) have been the more controversial stages of the transition process. It is during these stages that the primary vortex loop, or Λ-vortex, is observed to form and develop in flow-visualization experiments (Hama, Long & Hegarty 1957). The seventh and eighth steps occur as the high-shear layer begins to break down. The idea that the high-shear layer is sensitive to disturbances with frequencies higher than the Tollmien–Schlichting wave was originally proposed by Betchov (1960) and investigated in more detail by Greenspan & Benney (1963) in terms of a secondary instability. The formation of turbulent spots and the subsequent coagulation of the spots (the last two stages) which form the turbulent boundary layer was first observed by Emmons (1951).

The focus of attention of this paper is on stages V and VI. Some attempts have been made to model the flow field in this region. Perhaps the most successful approaches have been by numerical methods. A numerical solution of the three-dimensional Navier–Stokes equations has been recently computed by both Orszag & Kells (1980) and Kleiser (1982) for a temporally amplifying disturbance in plane Poiseuille flow. Their results predict a longitudinal vorticity field similar to that measured in the boundary layer on a flat plate. Similar results have been obtained for the Blasius flow by Wray & Hussaini (1980). Although one must be cautious in interpreting the results obtained from a calculation that assumes spatial periodicity, it does appear that numerical solutions of the complete Navier–Stokes equations are making significant progress towards computing the transition process.

The vortex-loop concepts, which are primarily based on flow-visualization experiments, began with Theodorsen's (1955) proposal that the horseshoe vortex might be a fundamental unit of turbulence. Hama *et al.* (1957) used dye to visualize the transition process, and concluded that the vortex loop was indeed the primary structure of the disturbance during the three-dimensional stage of transition. The hydrogen-bubble flow-visualization technique was used by Hama & Nutant (1963) to refine the vortex-loop concept, and show that the primary vortex loop created the instantaneous high-shear layer that leads to the formation of hairpin vortices. However, these experiments lacked the quantitative detail necessary to conclusively prove the existence of the vortex loop.

Other experiments were conducted to clarify the three-dimensional structure.

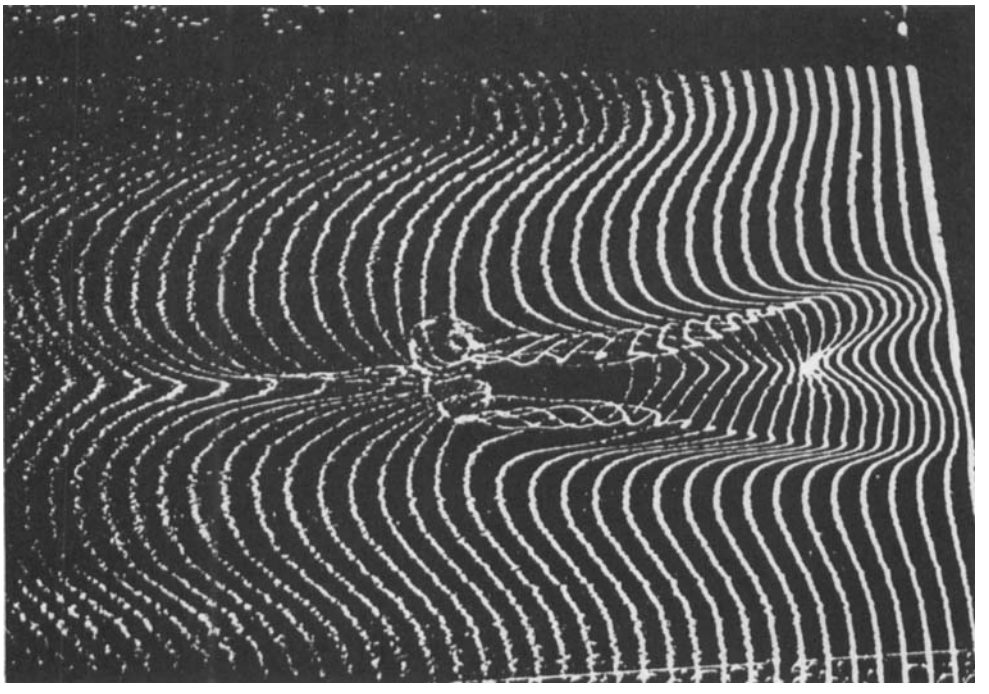

FIGURE 1. Photograph of hydrogen bubbles showing the vortex loop near $X = 60$ cm shortly before the formation of hairpin eddies. The flow is from right to left. The hydrogen-bubble wire is positioned close to the critical layer.

Klebanoff, Tidstrom & Sargent (1962) measured the streamwise and spanwise velocity components in great detail using hot-wire anemometry, and were able to identify the presence of streamwise vorticity in the flow field. Kovasznay, Komoda & Vasudeva (1962) measured all three velocity components, and concluded that a low-speed fluid 'bump' was responsible for the high-shear layer formation. Tani & Komoda (1962) and Komoda (1967) investigated the effects of spanwise periodicity of the mean flow on the transition process, and found that the characteristics of the disturbance could be altered. Based on a flow-visualization study, Wortmann (1977) proposed a slightly different concept, which he described as a 'roof-shingle' arrangement of the original vortex loop and secondary 'antiloop'.

The purpose of this sketchy summary of investigations into stages V and VI is to illustrate the current understanding (or lack of it) of the nonlinear three-dimensional stage of transition. Clearly, there is no general agreement on the physical mechanisms leading to breakdown of the laminar boundary layer. With the current availability of laboratory computers and efficient digital data-analysis techniques, we felt that it would be possible to clarify the flow structure, and hence the transition mechanism at this state of development. Indeed, it was the goal of the present experiment to resolve unequivically the true three-dimensional structure of the disturbance before the breakdown stage, by quantitatively mapping all three components of the instantaneous velocity and vorticity fields.

In order to illustrate some of the terms used in this paper, a photograph (taken by Stephan de la Veaux) of a vortex loop that formed during stages V and VI is shown in figure 1. The hydrogen bubbles show the loop shortly before the formation of hairpin eddies. The 'tip' region is the centre portion of the loop, which connects the

two 'leg' regions. The tip is situated higher in the boundary layer and travels downstream faster than the legs. The leg regions appear to contain large streamwise components of vorticity.

In §2 of this paper the experimental parameters, data-acquisition and data-analysis techniques that were used in this study are described. This is followed in §3 by a presentation of the time-averaged results of the flow field, which includes mean velocity and mean vorticity. The time-averaged properties of the disturbance are examined in §4. Section 5 is primarily concerned with the instantaneous vorticity field. In §5.1 the vorticity associated with the vortex loop is examined, while in §5.2 the vorticity field surrounding the loop and the corresponding inflexional high-shear layer development are considered. The conclusions are presented in §6.

2. Experimental details

The low-turbulence water channel used in this investigation was specifically designed for the study of boundary-layer transition. Its overall length was 14.6 m, with a test section width and length of 150 cm and 820 cm respectively. The boundary layer developed on the false bottom of the test section, which was a flat glass plate 0.64 cm thick. The water level above the plate was held at 17.5 ± 0.05 cm. In order to prevent separation on the plate surface, a 4:1 semi-elliptic leading edge was attached and given a slight downward angle. Flow visualization with dye ensured that the stagnation line occurred on the top side. The free-stream velocity U_0 was 10.05 ± 0.5 cm/s. The r.m.s. (root-mean-square) amplitude of the free-stream turbulence was reduced to less than $0.002U_0$ over the spectrum from 0.01 Hz to 1 kHz by inserting before the contraction a 1 m thick section of porous foam and three 5 cm thick honeycomb sections. The water temperature was 25.5 ± 0.6 °C.

An initially two-dimensional disturbance was introduced into the boundary layer by oscillating a 0.25 mm diameter tungsten wire, which spanned the entire width of the test section. Tests using a laser beam reflected from the wire showed the motion of the wire to be quite uniform. In this particular experiment the wire was located at 187 cm from the leading edge at a mean height of $Y = 0.5$ cm, and was driven by a mechanical lever–cam arrangement. The motion of the lever was measured by a linear transducer for use as a reference signal during the data acquisition and analysis. The wire itself was stretched very tightly to ensure that the amplitude was uniform across the span, and to avoid any distortion caused by the loading of the flow. The frequency of the wire oscillation was 0.263 Hz, which corresponded to a non-dimensional frequency parameter $F = 2\pi f\nu/U_0^2 = 1.44 \times 10^{-4}$, where f is the frequency and ν the kinematic viscosity. By extrapolation from the disturbance amplitudes at downstream locations, the amplitude of the disturbance at the wire was estimated to be $0.01U_0$. Such a large initial amplitude was used to ensure that the disturbance development was highly repeatable. No attempt was made to control artificially the three-dimensional development of the disturbance.

By using the hydrogen-bubble flow-visualization technique, the transition process in this experiment was identified to be the same as that observed by Hama & Nutant (1963). The velocity-measuring locations formed a rectilinear volume, which was laterally centred at the location where the tip of the vortex loop appeared. This measuring volume consisted of eight streamwise (X-axis, u-velocity) locations ranging from 35 to 70 cm from the wire in increments of 5 cm. In the spanwise direction (Z-axis, w-velocity) were eight measuring stations, which covered a 4 cm width. Normal to the plate (Y-axis, v-velocity) were 16 measuring locations over a

3.05 cm height for the spanwise velocity component measurements. When the vertical velocity component was measured only 14 measuring locations could be reached, due to physical limitations of the vertically oriented probe near the plate. In this paper the total velocity is represented by a lower-case letter, the mean velocity by a capital letter, and the fluctuating component with a primed lower-case letter, e.g. $u = U + u'$. The same notation is used for vorticity.

All three velocity components were measured at each grid point in the measuring volume using constant-temperature hot-film anemometers. The probes were the slant-film type, and were operated at 7 % overheat ratio. Although this is a relatively low overheat ratio, it was more than adequate to resolve the highest frequencies encountered, and low enough to prevent air bubbles from forming on the probe sensor. Nevertheless, an extensive and frequent de-aeration, as well as a three-stage filtering of the water, was required to reduce the size of the foreign particles and dust to less than 0.2 μm, thus ensuring a quantitatively repetitive performance of the probe.

In order to obtain the instantaneous cross-flow velocity components (v, w), the slanted probe sensor must be oriented in two different directions for each cross-flow component, and the corresponding cooling-velocity signals subtracted at each instant in time. To do this a phase-averaged cooling-velocity signal was computed for each of the four probe orientations required (two in the (X, Z)-plane and the other two in the (X, Y)-plane) at each grid point. In this way the probe could be placed at exactly the same point, although the orientation of the sensor was changed. Next the phase-averaged u-, v- and w-velocity components could be computed over one cycle of the disturbance oscillation after the cooling-velocity signal that represented the average disturbance signal at the grid point was found. The phase equal to zero position was taken to be the instant when the reference signal crossed zero with a positive slope.

The hot-film probes were calibrated by towing them through a small towing tank at speeds ranging from 0.5 to 15.0 cm/s. A fourth-order polynomial was fitted to the calibration curve of $E - E_0$ against cooling velocity u_{cool}, where $E - E_0$ is the difference between the bridge voltages when the probe is moving and at rest. The cooling velocity had been determined from $U_{\text{cool}} = U \cos \alpha_{\text{eff}}$, where U was the probe speed and α_{eff} was the effective angle of the sensor as determined by a direct calibration similar to Bradshaw's method (1971).

The conditional-sampling program used to determine the phase-averaged signal took advantage of the repeatability of the flow field, and, since the flow developments were not exactly repetitive, a data-selection scheme was required. A band of acceptance based on the standard deviation of the amplitude and phases of the voltage minima was set, and only those signals that met the amplitude and phase criteria were used for the averaging. The variance between the individual signals at any particular phase angle was, in most cases, an order of magnitude lower than the variance over one cycle of the phase-averaged signal. Thus the phase-averaged signal accurately represented the instantaneous signals. From the phase-averaged signal the cooling velocities could be calculated; then the streamwise and crossflow velocity components were computed.

The vorticity at a given grid point was computed from the velocity components using the so-called central-differencing technique. The three vorticity components Ω_X, Ω_Y and Ω_Z were computed at each grid point for various phase instants over one cycle. When contours of vorticity were plotted, a linear interpolation was used between the grid points.

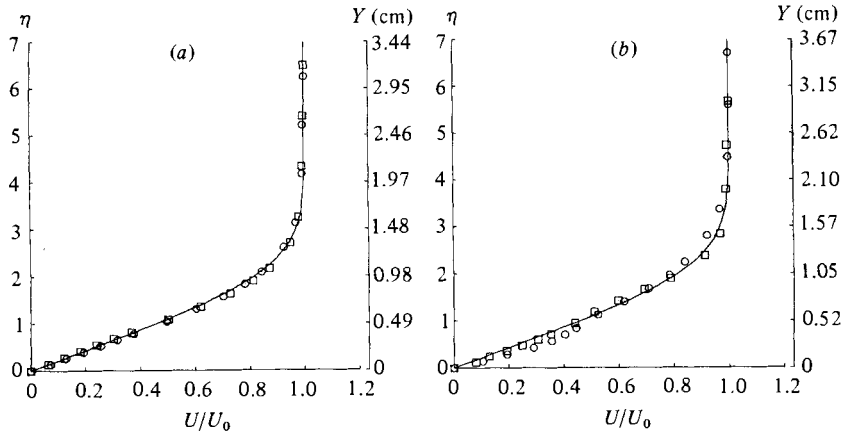

FIGURE 2. Mean-velocity profiles at two spanwise locations compared with the Blasius profile: □, $Z = 0$ cm; ○, -1.5 cm; solid line is the Blasius profile: (*a*) $X = 40$ cm; (*b*) 60 cm.

3. Mean-flow field

The mean longitudinal velocity profiles and comparison with the Blasius profile at locations $X = 40$ cm and $X = 60$ cm from the oscillating wire are shown in figures 2(*a*, *b*). The solid line is the Blasius profile, where the left ordinate is $\eta = 1.72Y/\sqrt{2}\,\delta^*$ and the abscissa is U/U_0. The measurements were made with the disturbance present. The displacement thickness δ^* was determined by integrating the velocity defect of each experimentally measured velocity profile from the wall to the highest point measured in the free stream, $Y = 3.05$ cm. The ordinate on the right-hand side of the plots in figures 2(*a*, *b*) is an approximation to the dimensional height in centimetres. The symbols □ and ○ show the experimentally measured velocities at two spanwise locations $Z = 0$ and $Z = 1.5$ cm, which correspond respectively to the centre and side regions of the disturbance.

The velocity profiles at the $X = 40$ cm location represent the early nonlinear stage of development, where the disturbance u'_{rms} amplitude maxima were approximately $0.055U_0$. At both spanwise locations, the mean profiles are very close to the Blasius profile, even though the disturbance amplitude is already large enough for nonlinear effects to be present. The critical layer, a concept that originates from linear stability theory (and which is defined as the height where the mean-flow velocity equals the

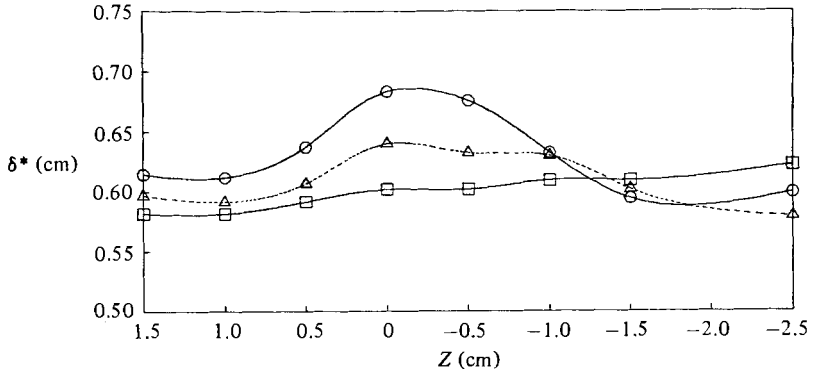

FIGURE 3. Spanwise variation in displacement thickness for different streamwise locations: □, $Z = 40$ cm; △, 50 cm; ○, 60 cm.

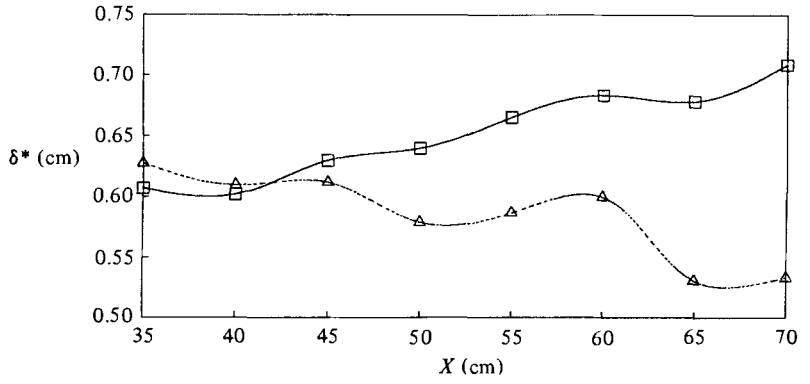

FIGURE 4. Streamwise variation in displacement thickness for two spanwise locations: □, $Z = 0$ cm; △, -2.5 cm.

disturbance wavespeed), is used in this report as a reference height within the boundary layer. The disturbance reaches its maximum amplitude $u'_{\text{rms}} = 0.14U_0$ at $X = 60$ cm, at which point the mean-velocity profiles are inflexional.

As the disturbance develops in the downstream direction, it causes an appreciable non-uniformity in the displacement thickness across the span, as shown in figure 3. Since the measuring volume was so chosen to focus on the more active disturbance developments occurring near the spanwise centre of the volume, where a fine spanwise spatial resolution was required, its width did not cover the entire spanwise

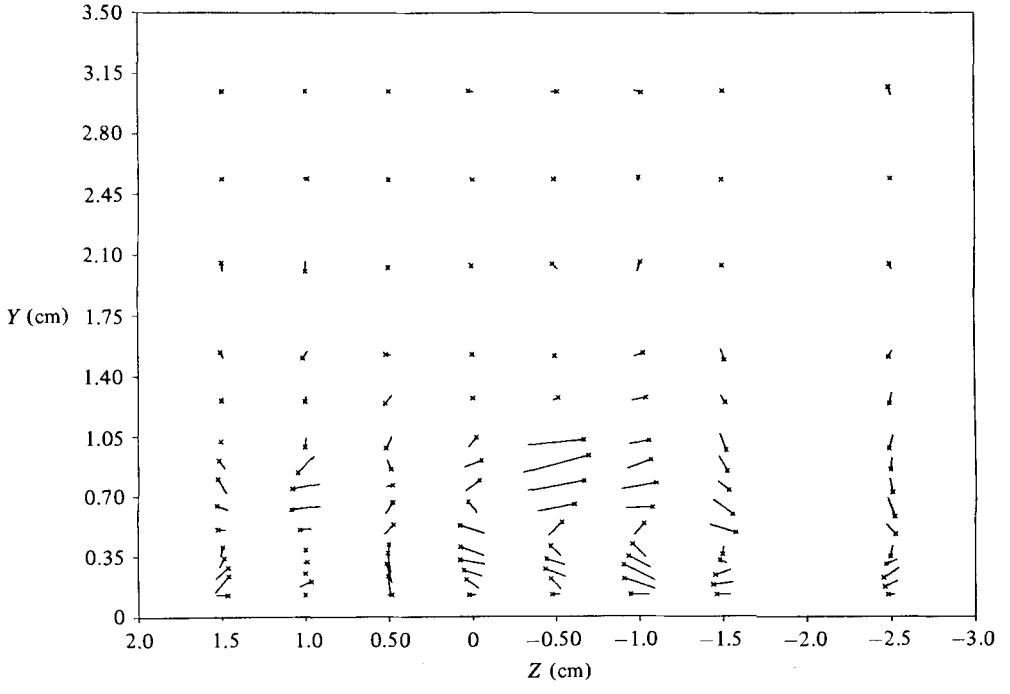

FIGURE 5. Projection of mean-flow velocity vectors on the (Y, Z)-plane at $X = 60$ cm. The tip is distinguished from the tail of the vector by a small ×. The vectors have been centred over the measuring point.

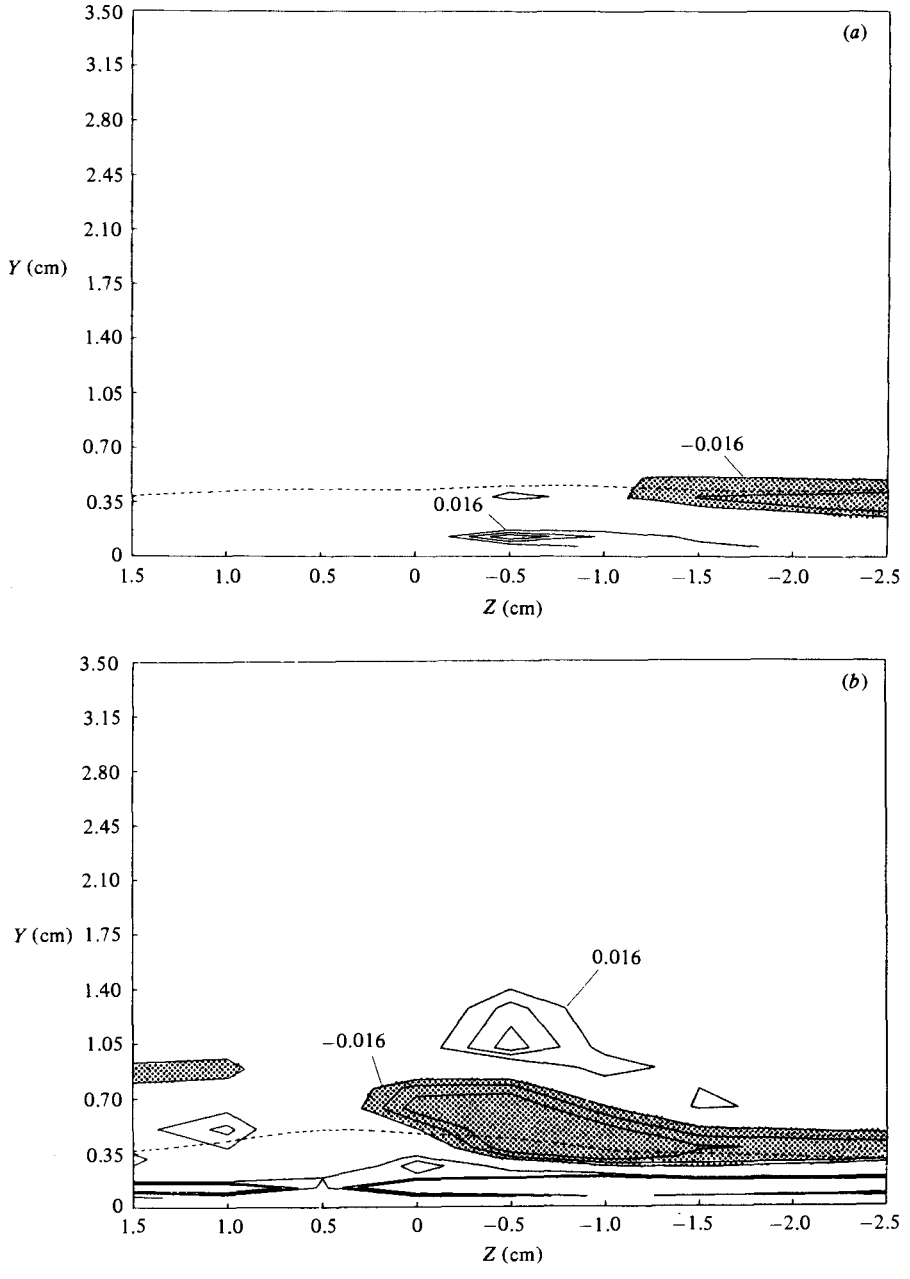

FIGURE 6. Contours of mean streamwise vorticity Ω_X plotted in the (Y, Z)-plane at $X = 60$ cm: (*a*) $X = 40$ cm; (*b*) 60 cm. – – – –, critical layer; ——, contours of $\Omega_X = \pm 0.047, \pm 0.032, \pm 0.016$. The regions of negative vorticity have been shaded.

wavelength. The displacement thickness increases more rapidly around $Z = 0$ than at the other spanwise locations; thus by $X = 50$ cm a local maximum in δ^* exists in the spanwise centre. The downstream variation in δ^* is more clearly shown for $Z = 0$ and $Z = -2.5$ cm in figure 4. While δ^* steadily increases along the centreline, it decreases along $Z = -2.5$ cm at the later stages of the development. The Reynolds number based on δ^* varies along the centreline from 711 to 850.

The spanwise variation in δ^* can be explained by the effects of a counterrotating pair of mean longitudinal vortices acting on the mean-flow field. These vortices sweep low-momentum fluid toward the spanwise centre of the disturbance, causing the displacement thickness to increase in a manner described by Stuart (1965). The circulation about the vortex pair, one on either side of $Z = 0.5$ cm, can be seen in figure 5, which shows the projections of the mean-velocity vectors (w, v) in the plane normal to the flow direction ((Y, Z)-plane) at $X = 60$ cm. The mean-flow field is not exactly symmetric, with the stronger longitudinal vortex in the $Z < 0$ side, which is believed to be a result of the non-uniformity in the undisturbed mean-flow field. The flow below the critical layer moves toward the spanwise centre, where it turns upward, carrying the low-momentum fluid away from the plate. The displacement thickness increases, because the momentum deficit in the velocity profile is increased by this accumulation of low-momentum fluid. Along $Z = -2.5$ cm the opposite situation occurs and the displacement thickness decreases with downstream distance because the longitudinal vortices bring the high-momentum fluid down closer to the plate.

The mean longitudinal vorticity $\Omega_X = \partial W/\partial Y - \partial V/\partial Z$ has been computed from the mean transverse and vertical velocity components at $X = 40$ cm and $X = 60$ cm. The corresponding contours of constant Ω_X, which have been normalized by $U_0/\bar{\delta}^*$ ($\bar{\delta}^*$ is the average displacement thickness across the measuring plane at a fixed streamwise location), are plotted in figures 6(a, b). The approximate location of the critical layer is indicated by a broken line, which shows that at both streamwise locations the maxima are approximately centred on the critical layer. Further comparison of the contours of constant Ω_X in figures 6(a, b) shows that Ω_X increases in magnitude as the disturbance develops downstream. The centres of the counter-rotating components move towards the spanwise centre of the disturbance. At $X = 60$ cm a second pair of counterrotating vortices is observed farther from the plate above the original vortex pair centred on the critical layer.

4. Time-averaged properties of the disturbance

This section is concerned with the description of the disturbance in terms of the $u'_{\rm rms}$ amplitude distributions and the phase distributions of the fundamental and second harmonic. All three velocity components have been measured and more detailed information concerning v' and w' can be found in Williams (1982). The same two streamwise locations are considered as before, the $X = 40$ cm location representing the earlier stage of nonlinear development, while $X = 60$ cm is just prior to the disturbance breakdown.

To show the development of the disturbance amplitude across the boundary layer and its variation across the span as the disturbance travels downstream, the profiles of the $u'_{\rm rms}$ amplitude (expressed as percent of U_0) are plotted against Y for $X = 40$ cm and $X = 60$ cm in figures 7(a, b). At the earlier stage of disturbance development, $X = 40$ cm, the $u'_{\rm rms}$ profiles are almost independent of the spanwise location across the measuring volume. Even though the disturbance is nonlinear, with an amplitude maximum $u'_{\rm max}$ close to $0.055U_0$, the profiles still resemble the linear-stability theory predictions.

By the time the disturbance has reached its maximum amplitude at the downstream location of $X = 60$ cm, the profiles have become strongly dependent on the spanwise position. The local $u'_{\rm rms}$ maxima occur above the critical layer, reaching magnitudes as large as $0.14U_0$. The height of the local $u'_{\rm rms}$ minimum has increased slightly to

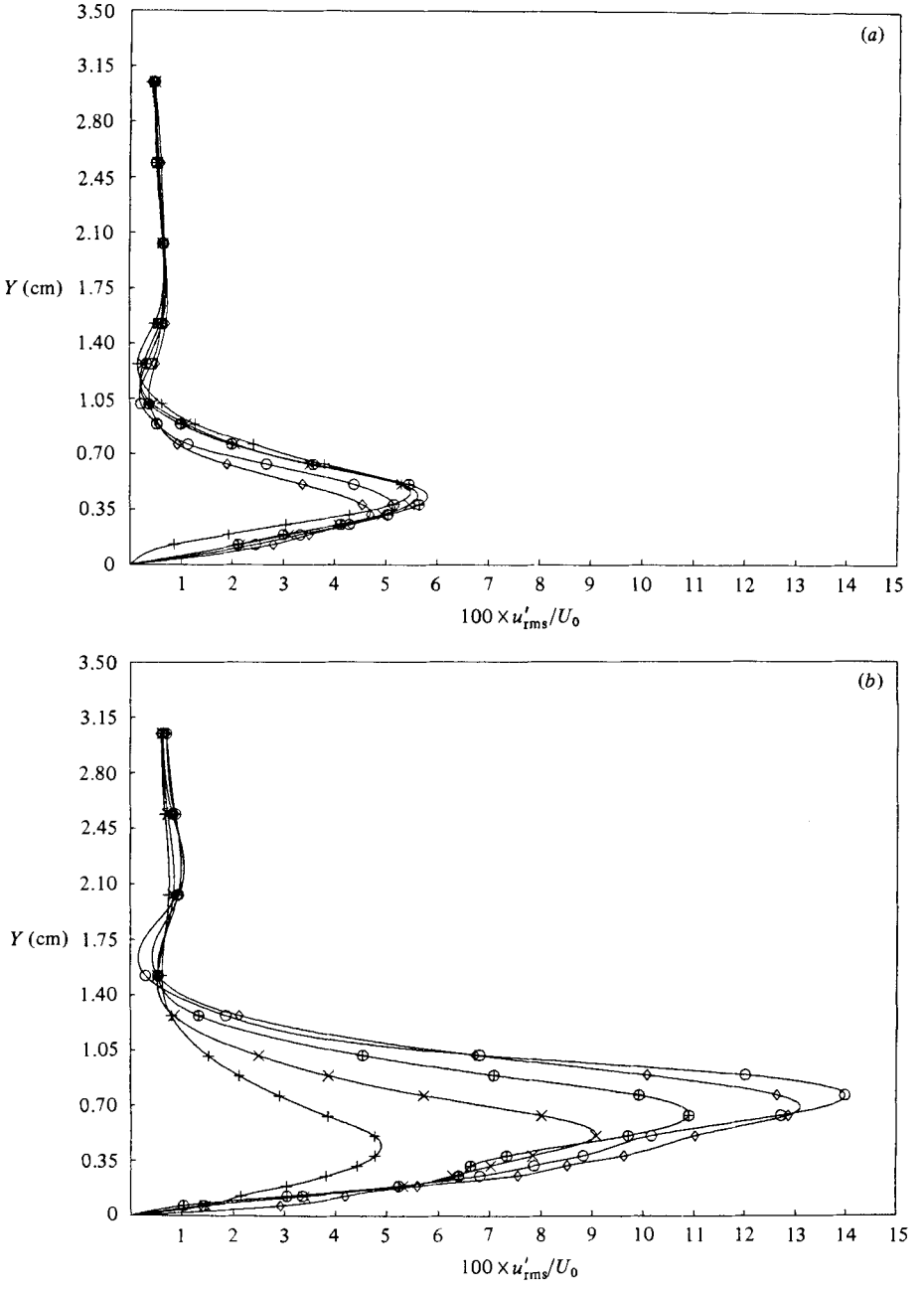

FIGURE 7. Distributions of u'_{rms} across the boundary layer for several spanwise locations. (*a*) $X = 40$ cm; (*b*) $X = 60$ cm. ◇, $Z = 0$; ○, -0.5; ⊕, -1.0; ×, -1.5; +, -2.5.

$Y = 1.5$ cm, but, more significantly, above this point no appreciable change in the amplitude distribution has occurred. It is quite interesting that the local amplitude maximum outside the boundary layer near $Y = 2.1$ cm remains about $0.01U_0$ for both downstream locations. Thus the major disturbance developments occur below the 180° phase-shift point in the boundary layer.

In order to reveal how the spanwise variation of the disturbance develops, the local maxima of u'_{rms} are plotted against Z in figure 8 for each downstream location

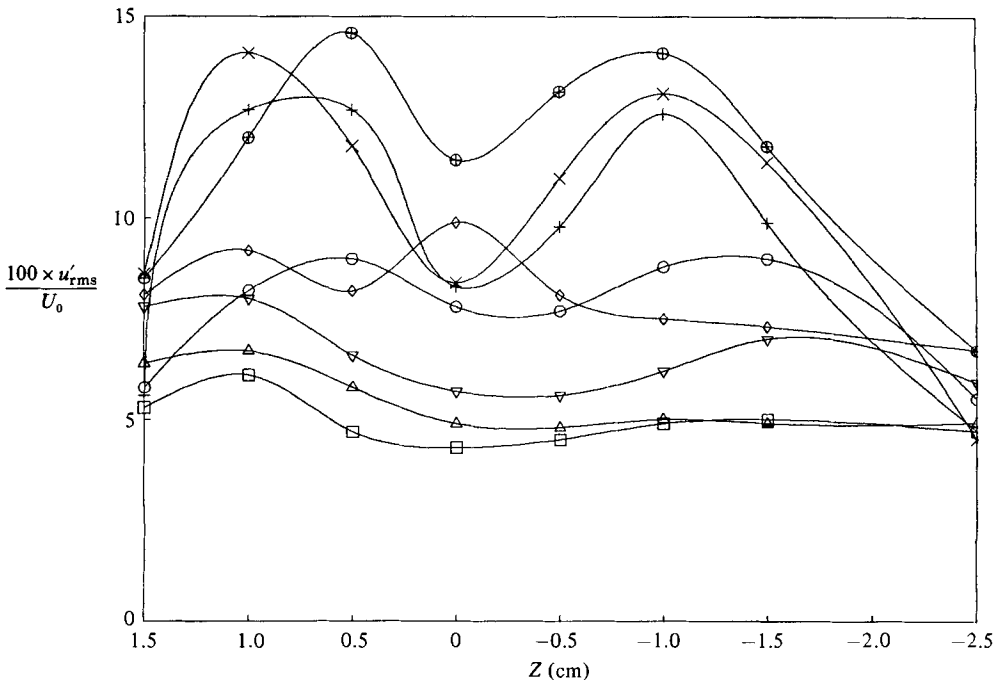

FIGURE 8. Variation of u'_{rms} maxima across the span for several streamwise measuring stations: □, $X = 35$ cm; △, 40; ▽, 45; ◇, 50; ○, 55; ⊕, 60; ×, 65; +, 70.

measured. The amplitude variation across the span is bimodal. The local amplitude maxima occur at $X = 60$ cm for two peaks in the spanwise direction $Z = 0.5$ cm and -1.0 cm. From this point on, the u'_{rms} amplitude maxima decrease as the disturbance breaks down toward a turbulent state.

The velocity signals can also be analysed in terms of the amplitude and phase distributions of the harmonic components present. The phase distributions in the downstream and transverse directions of the Fourier components are particularly interesting, because they provide the information about the shape of the wavefront and the wavespeed of the disturbance. These results show how the wavefront is distorted across the span (wavefront warping), and how the distortion increases as a result of varying phase velocities across the span.

The u' fundamental phase variation across the boundary layer is shown, for example, in figures $9(a, b)$ for the streamwise location $X = 60$ cm. Each profile corresponds to a different spanwise location. Some general characteristics of all the phase distributions measured can be identified in these profiles. Above the phase-shift height the phase values are uniform in both the spanwise and vertical directions. Below this level the phase angles change rapidly. The uniform phase in the higher part of the boundary layer is believed to characterize the global features of the disturbance, and was used in computing the overall wavespeed. The phase in the lower region exhibits a more localized and detailed behaviour, which provides information on the local phase velocities and wavefront warping.

Of primary interest is the variation of the phase in the downstream direction, since it is required to compute wavelengths and phase velocities, i.e. $\lambda = -\partial X/\partial\phi$ and $c_{ph} = f\lambda$, where λ is the wavelength, c_{ph} the phase velocity and ϕ the phase angle. The phase angles of the fundamental and the second harmonic of the u' disturbance

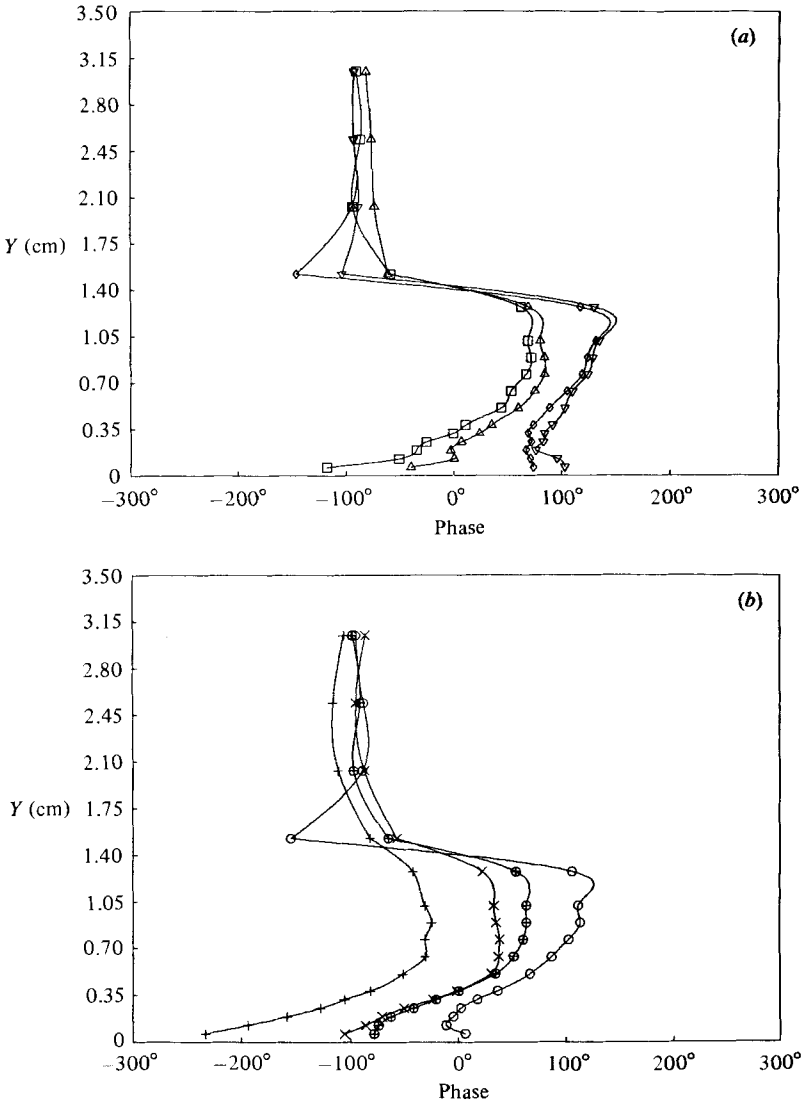

FIGURE 9. Distribution of u' fundamental phase across the boundary layer for several spanwise locations at $X = 60$ cm. (a): □, $Z = 1.5$ cm; △, 1.0; ▽, 0.5; ◇, 0. (b): ○, $Z = -0.5$ cm; ⊕, −1; ×, −1.5; +, −2.5.

at $Z = 0$ are plotted against the downstream location in figure 10. The phase of the fundamental is shown for two different vertical locations, one above the boundary layer, $Y = 2.54$ cm (box symbols), and the other inside the boundary layer where the u' fundamental amplitude is maximum (triangles). The phase of the second harmonic of u' (circles) is also measured at the location where its amplitude is a maximum. The wavelength λ_f, of the fundamental oscillation, computed from the free-stream phase variation, shows $\lambda_f = 16.2$ cm, and the corresponding phase velocity $c_{ph} = 4.2$ cm/s. The phase of the u' fundamental disturbance inside the boundary layer changes slightly less rapidly; consequently, the wavelength is a little longer and the wavespeed a little faster, $\lambda_f = 17.5$ cm and $c_{ph} = 4.5$ cm/s. Thus the wavespeed of the fundamental is in fact dependent on the height inside the boundary layer.

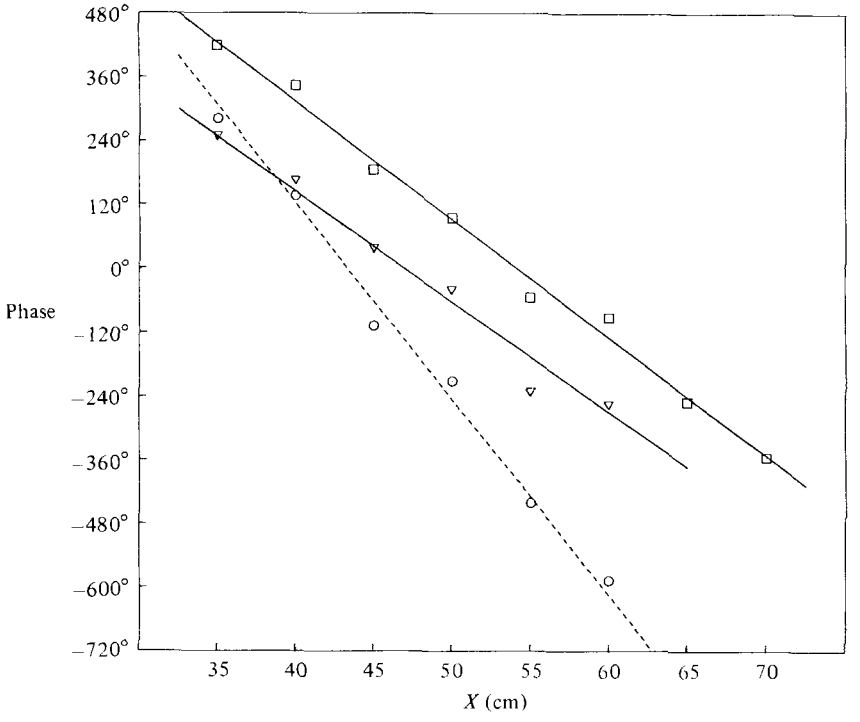

FIGURE 10. Streamwise phase variation of the u' velocity; ▽, phase of the fundamental at $Y = 2.54$ cm; □, phase of the fundamental at the height of amplitude maximum of the fundamental; ○, phase of the second harmonic at the height of amplitude maximum of the second harmonic.

The downstream gradient of the second-harmonic phase is about twice that of the fundamental. The corresponding wavespeed of the second harmonic is $c_{ph2} = 5.3$ cm/s, which is within 15% of the wavespeed of the fundamental disturbance inside the boundary layer. Since the fundamental and the second harmonic have the same wavespeed, within reasonable accuracy, the initial phase difference between the two waves will not change, and the second harmonic essentially travels downstream along with the fundamental.

The next significant result of the phase measurements is seen in the u' phase variations in the spanwise direction, as shown in figures 11 (a, b). Flow-visualization experiments (Hama *et al.* 1957; Hama and Nutant 1963; Wortmann 1977) have consistently indicated that the wavefront of the disturbance warps across the span. The spanwise centre (peak) region of the disturbance appears to move faster downstream than the sides. The head of the Λ-vortex forms around the peak region, and the legs of longitudinal vorticity form on the sides. If the wavefront warping observed in the flow-visualization experiments is truly an indication of the disturbance-wavefront warping, then the u' phase should also vary across the span, and the spanwise phase variation should increase with increasing downstream distance. Indeed phase values for the u' fundamental and second harmonic, taken at the height in the boundary layer where the amplitude of each component is a maximum, clearly illustrate an increasing distortion of the wavefront from $X = 40$ cm to $X = 60$ cm. It is quite astonishing, on the other hand, that the disturbance in the free stream maintains a relatively uniform, essentially two-dimensional phase distribution across the span at both locations. This observation has a serious implication that, even

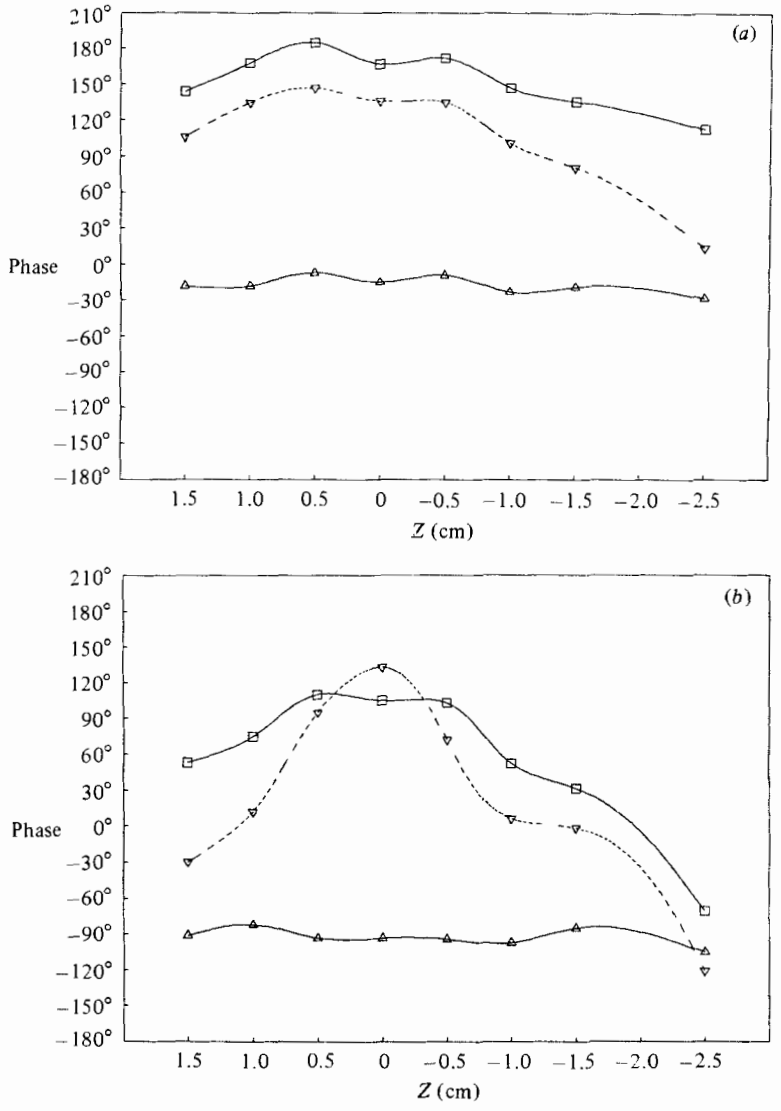

FIGURE 11. Variation of u' phase across the span: △, phase of the fundamental at $Y = 3.05$ cm; □, phase of the fundamental at the height of amplitude maximum of the fundamental; ▽, phase of the second harmonic at the height of amplitude maximum of the second harmonic.

though the wave develops quite three-dimensionally inside the boundary layer (below the 180° phase-shift point), an observer in the outer part of the boundary layer will be unable to recognize this development. Furthermore, even when an observer recognizes three-dimensionality in the outer flow, the true three-dimensional structure inside the boundary layer could be totally different from what he imagined.

The increase in wavefront warping is explained by a dependence of the phase speed on spanwise location. The phase speed at $Z = 0$ is slightly faster than that of the disturbance outside of the boundary layer, the outer-flow disturbance, which remains constant across the span. As a result, the phase difference between the inner boundary layer and outer-flow disturbances, $\Delta\phi = \phi_{\text{inner}} - \phi_{\text{outer}}$, increases from $\Delta\phi = 180°$ at $X = 40$ cm to 210° at $X = 60$ cm. In contrast, the disturbance inside the boundary

layer along $Z = 2.5$ cm travels slower than the outer-flow disturbance, which causes the phase difference to decrease from $\Delta\phi = 135°$ at $X = 40$ cm to $\Delta\phi = 30°$ at $X = 60$ cm. Since the phase speed of the free-stream disturbance is uniform across the span, the differing phase speeds of the u' fundamental inside the boundary layer cause the wavefront to warp further as the disturbance travels downstream. This varying phase velocity may also be a result of the vorticity concentration, as described later. In the earlier stage of the development, which may be described by the linear stability theory, the vorticity fluctuations are essentially due to the wavy motions inside the boundary layer, and the propagation velocity is the wave velocity. Once the vorticity is concentrated, however, its propagation velocity becomes the local convection velocity, which differs depending on the locations, particularly the vertical height.

The spanwise phase variations of the second harmonic in the boundary layer are shown as the dotted lines in figure 11 (*a*, *b*). As in the streamwise case, the phase variation of the second harmonic is approximately twice as large as the fundamental. Thus the second harmonic travels downstream with the same phase speed as the fundamental, not only along the spanwise centre of the disturbance, but also off-centre, where the phase speed of the disturbance decreases. The position of the second harmonic relative to the fundamental is independent of spanwise or streamwise location, and the nonlinear effects are said to 'ride' on the fundamental.

5. Instantaneous vorticity field

5.1. *The vortex loop*

In order to describe the structure of the flow field, the velocity and vorticity fields have been computed and presented in terms of the total components, i.e. the mean plus fluctuating terms. In this subsection the existence of the vortex loop will be shown by examining the longitudinal component of vorticity in the neighbourhood of the critical layer. In §5.2 the vorticity field surrounding the loop will be discussed. As in the mean-flow case, all vorticity values have been normalized by $\bar{\delta}^*/U_0$. The three-dimensionality of the disturbance and the intensity of its streamwise vortices are most pronounced, and hence most clearly seen, at $X = 60$ cm. The structure of the disturbance upstream of $X = 60$ cm, although not as highly developed, is quite similar. Thus only data at $X = 60$ cm are presented in §5, because they are representative of the data at the upstream stations.

The first indication of the structure of the vortical disturbance is seen in the contours of constant longitudinal vorticity in the (Y, Z)-plane normal to the mean-flow direction in figures 12 (*a–f*). This is equivalent to looking upstream and watching the disturbance move through the measuring plane as the phase angle of the reference signal increases in increments of 60°. The vorticity contours are superposed on the instantaneous-velocity vectors, which show the w- and v-components. The solid contours have values of vorticity that range from $\omega_X = -0.252$ to -0.063, and the dashed contours range from $\omega_X = 0.063$ to 0.252, both in increments of 0.063. The velocity vectors show the sense of the circulation around the maxima of ω_X. It is clear that a pair of counterrotating streamwise vortices exist in the instantaneous flow field from phase 0° to 180° with centres near the critical layer ($Y = 0.5$ cm). The longitudinal vortex with negative ω_X is slightly stronger in magnitude than its positive counterpart, which indicates that the flow field is not exactly symmetric. As the phase angle increases, the centres of the ω_X maxima move sidewise away from spanwise centre and downward closer to the plate.

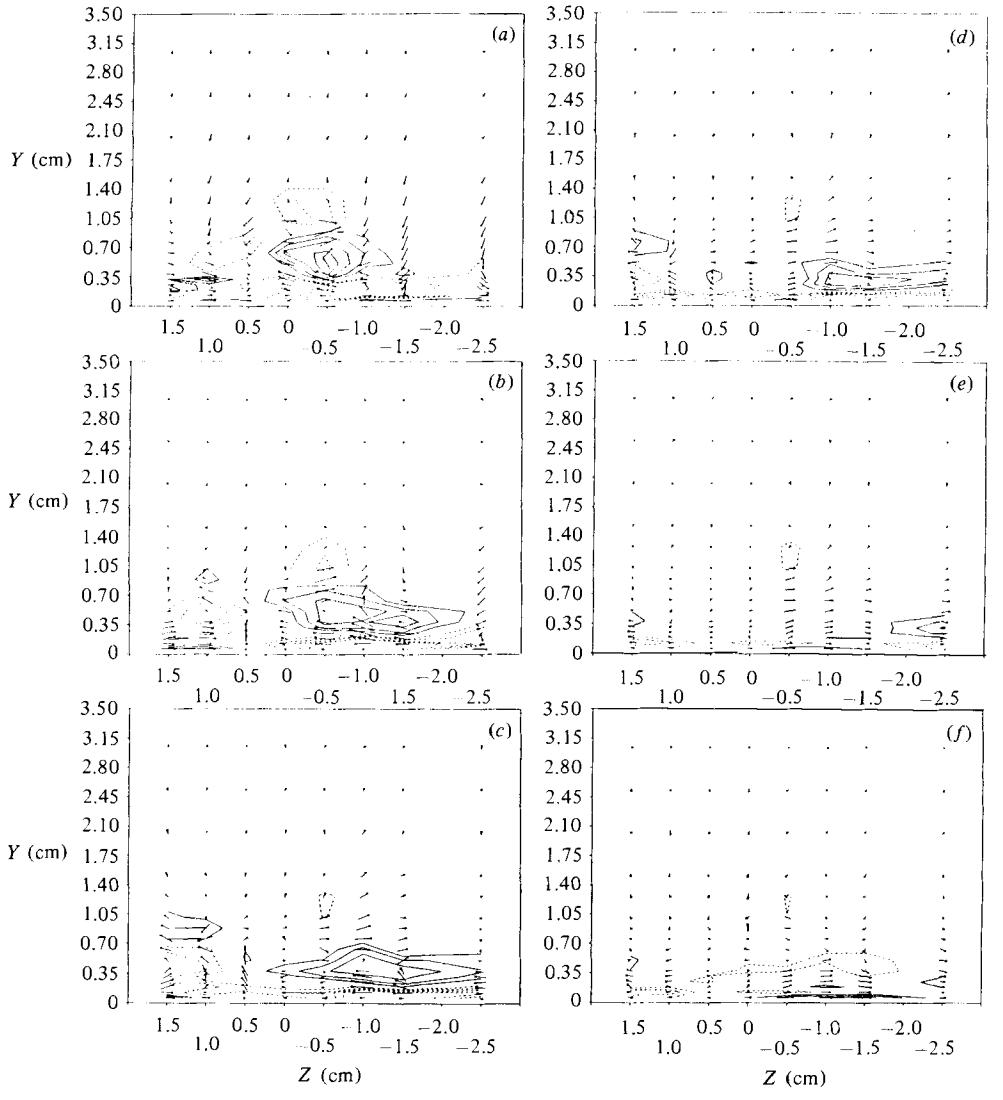

FIGURE 12. Contours of instantaneous streamwise vorticity superposed with the projections of the instantaneous velocity vectors in the (Y, Z)-plane at $X = 60$ cm. The solid lines are contours of positive vorticity and the dotted lines are the contours of negative vorticity. The time increment between plots corresponds to a 60° phase change of the fundamental oscillation. The contours are incremented by $\omega_X = 0.063$, beginning with $\omega_X = \pm 0.063$.

The same contours of streamwise vorticity plotted in figures 12(*a–f*) have been superposed on the corresponding instantaneous-vorticity vectors in figures 13(*a–f*). The vectors in these figures are the total instantaneous-vorticity vectors projected on to the (Y, Z)-plane. It is significant that the locations of the maxima of the ω_X vorticity component in the vicinity of the critical layer correspond to the local minima in the ω_Z component for phase angles 0°–180°. In other words, the ω_X component is dominant in this particular region, which means the vortex lines are oriented primarily in the streamwise direction. These longitudinally directed lines of vorticity form the two counterrotating cores of vorticity, which are located on either side of $Z = 0$. These cores of vorticity are recognized as the legs of the vortex loop that have

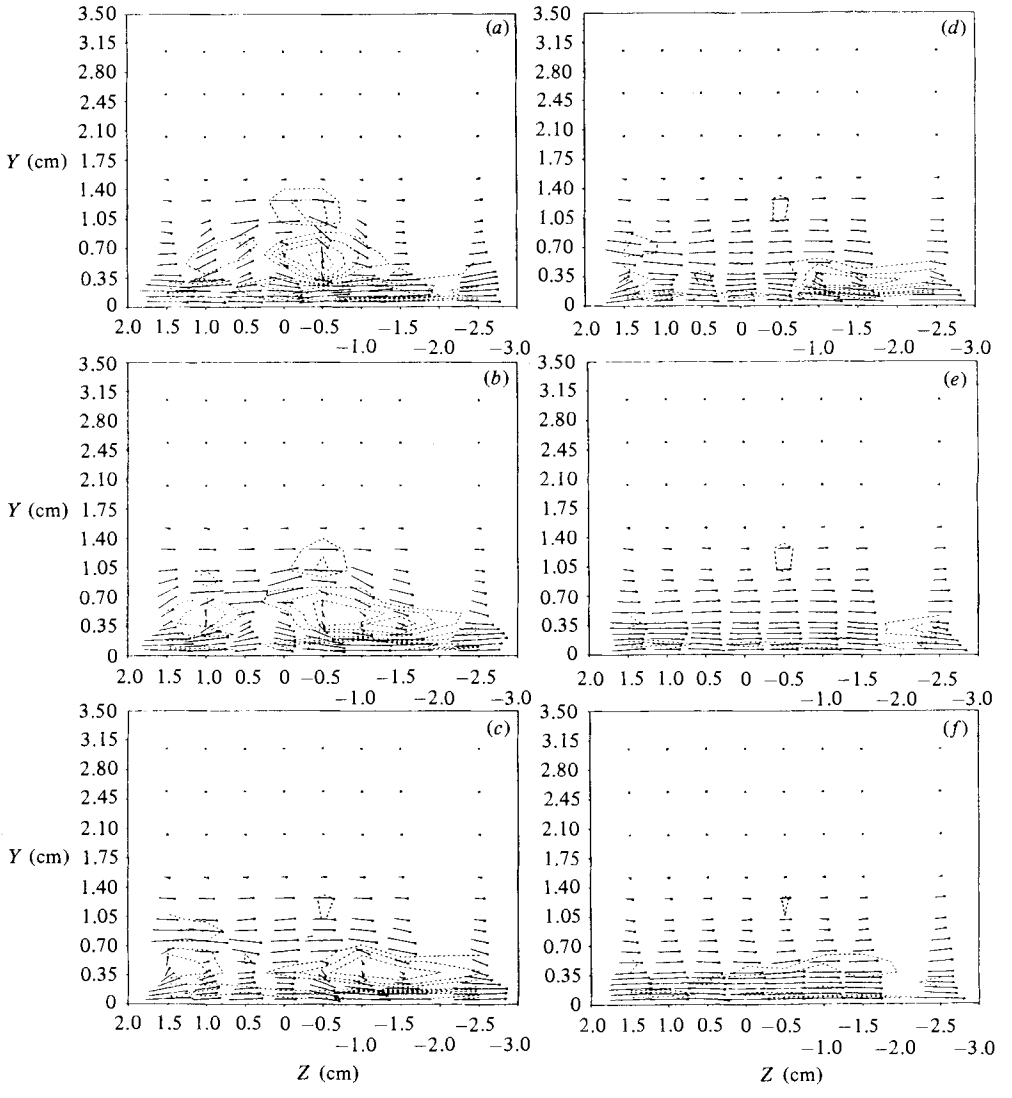

FIGURE 13. Contours of the instantaneous streamwise vorticity superposed with the projections of the instantaneous vorticity vectors in the (Y, Z)-plane at $X = 60$ cm. The contours are shown as the dotted lines. The vectors are centred over the measuring point, with a × indicating the tip of the vector.

been observed in flow-visualization studies. The ω_Y component of vorticity (observed in the vorticity vectors, figures 13*a–f*) also agrees with the concept of a loop-shaped tube of vorticity, whose tip is higher in the boundary layer than the legs.

The apparent motion of the regions of strong ω_X, as the disturbance passes through the (Y, Z)-plane at $X = 60$ cm, suggests a Λ-shaped loop. The contours of constant streamwise vorticity ($|\omega_X| = 0.13$) plotted in a perspective view in figure 14 may more clearly depict its geometry. Here the X-axis has been replaced by $-t$, where t is the phase of the reference signal. The Taylor's hypothesis used here will not precisely describe the shape of the disturbance beyond $X = 60$ cm, as the flow field breaks down in that region. Preceding the breakdown, however, the shape of the disturbance

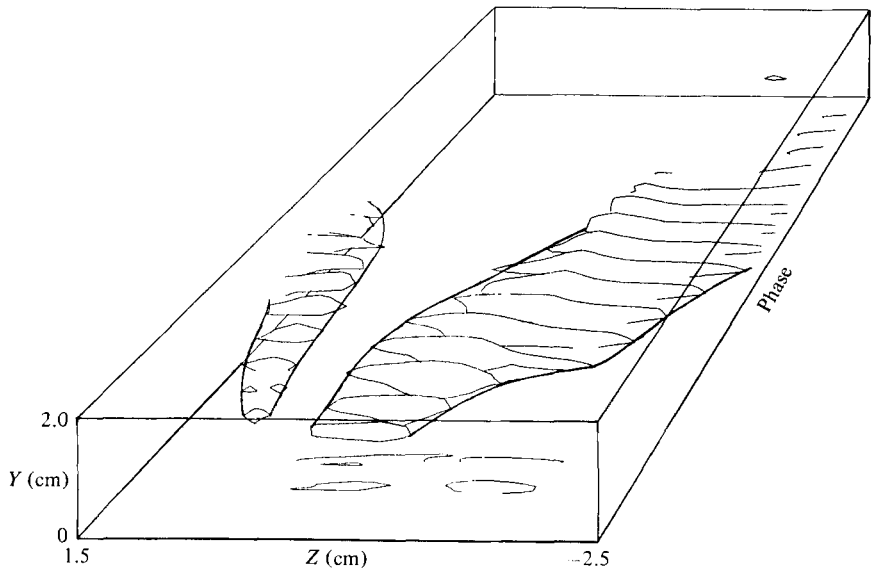

FIGURE 14. Perspective view of the legs of the vortex loop mapped by the streamwise-vorticity contour. $|\omega_X| = 0.13$. The flow direction is from the top right to lower left of the plot.

does not change drastically, and the approximation probably gives a reasonable spatial description of the disturbance.

The contours of longitudinal vorticity show that the strong component is confined to a region roughly 5 mm in vertical thickness and is more spread out (10–15 mm) horizontally. In the downstream direction (decreasing phase angle) the legs of the loop converge towards the spanwise centre $Z = 0$. The cores of vorticity, which form the legs of the loop, must connect in the tip region to close the loop. In the tip region, practically only the spanwise component of vorticity exists and ω_X disappears. The tip is not easily identified in contours of ω_Z vorticity, because the vorticity there is relatively weak compared with that in the other regions of the flow field. However, a large disturbance occurs in the v' velocity signal at approximately $t = -45°$, which results from the $\partial v/\partial X$ component of ω_Z and indicates that the tip of the vortex loop has just passed the measuring plane at that instant.

5.2. *Vorticity field around the loop*

The vorticity field surrounding the loop consists primarily of a strong ω_Z component of vorticity. The contours of ω_Z vorticity (solid lines) in the (Y, Z)-plane at $X = 60$ cm are shown in figures 15(*a–f*) for phase angles 0°–300°. The contours of constant ω_X vorticity (both positive and negative) are superposed as the dotted lines. The ω_Z contours have values ranging from -0.063 to -0.95 in increments of 0.189. The shaded areas correspond to regions of the strongest spanwise vorticity, $\omega_Z < -0.44$. The unshaded regions with closed ω_Z contours are local minima in which the spanwise vorticity is almost zero.

As previously shown, the maxima of ω_Z vorticity do not coincide with the maxima of ω_X. Furthermore, from figures 15(*a–f*) one finds that the vortex loop does not have the largest magnitude of vorticity in the flow field. A region of strong vorticity lies above the legs of the loop near $Y = 1.0$ cm, and a second pair of intense vorticity regions are found between the loop and the wall below $Y < 0.3$ cm. These regions

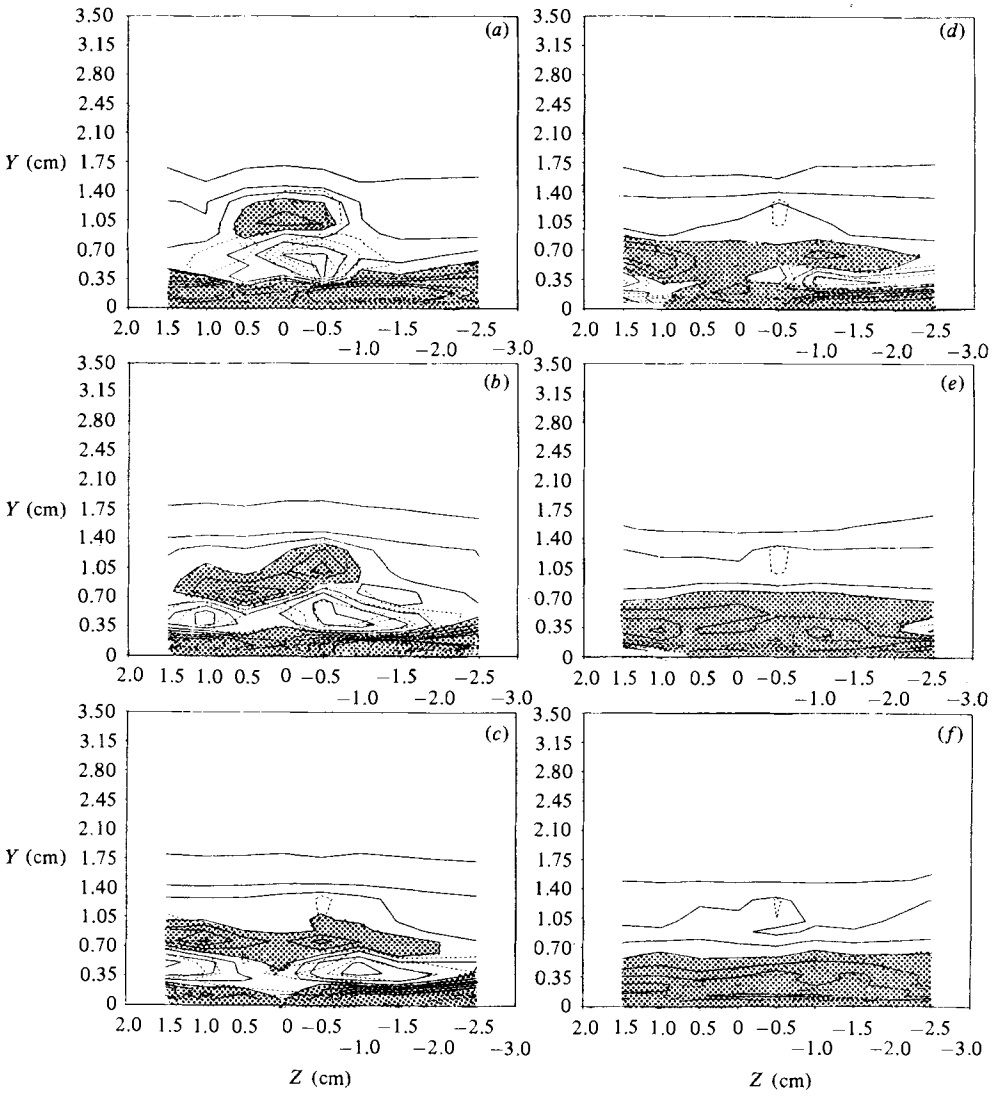

FIGURE 15. Contours of instantaneous spanwise vorticity (solid lines) ω_Z superposed with contours of streamwise vorticity (dotted lines) in the (Y, Z)-plane. The contours of spanwise vorticity are incremented by $\omega_Z = -0.19$ beginning with $\omega_Z = -0.06$. The phase angle is incremented by 60° between the figures. The shaded regions indicate $\omega_Z \leqslant -0.44$.

of vorticity only exist during the time the loop passes through the measuring plane, and they closely follow the apparent movement of the loop. The vorticity maxima near the wall reach magnitudes twice that of the undisturbed Blasius flow maximum, and three times the longitudinal vorticity maxima found in the legs of the vortex loop ($\omega_{X\max} = 0.3$).

The strong ω_Z component that lies above the vortex loop also appears in the vorticity vectors previously shown in figures 13(*a–f*). The vorticity-component configuration is inverted with respect to the vortex loop, i.e. the transverse component of vorticity, ω_Z, is at a local maximum, when the ω_X component is negligible. Thus the lines of vorticity above the vortex loop are oriented essentially

in the spanwise direction, almost at right-angles to the lines of vorticity in the legs of the vortex loop. Instead of forming a core as in the loop, the strong spanwise vorticity is spread out in a thin layer over about half the wavelength of the fundamental. Furthermore, the boundary between the lines of vorticity in the vortex loop and surrounding fluid is quite sharp, which distinguishes the two regions. Two structures are indeed present, the vortex loop and the layer of strong spanwise vorticity above it.

The physical significance of the strong vorticity layer above the loop can be clearly recognized when the contours of ω_Z vorticity are superposed on the instantaneous u-velocity profiles. In figures 16(a, b) the velocity profiles for two longitudinal cuts ((Y, T)-plane) at the spanwise locations $Z = 0$ and -1.5 cm show the spatial relationship between the large shear $\partial u/\partial Y$ and the maxima of ω_Z vorticity. The foot of the respective velocity profile on the abscissa gives its corresponding phase angle. The region of strong ω_Z vorticity above the vortex loop actually corresponds to the instantaneous inflexional high-shear layer in the velocity profiles. The experiments of Klebanoff *et al.* (1962), Kovasznay *et al.* (1962), Hama & Nutant (1963) and Nishioka, Asai & Iida (1980), along with the theories of Betchov (1960) and Greenspan & Benney (1963), have shown that the inflexional high-shear layer is sensitive to high-frequency disturbances, which lead to the formation of hairpin vortices during the breakdown stage.

How the inflexional high-shear layer forms can be determined by examining the velocity vectors observed from a reference frame that travels downstream with the speed of the outer-flow disturbance. Such a moving reference frame reveals the true structure of the disturbance flow field, which cannot be seen from the fixed-frame system (Hama, Williams & Fasel 1980). In figures 17(a, b) the projections of the instantaneous velocity vectors in the (Y, T)-plane at $Z = 0$ and -1.5 cm (superposed with velocity profiles) clearly illustrate how the faster-moving fluid travels around the vortex loop. The circle in figure 17(a) represents the approximate location of the tip of the vortex loop at $t = -45°$.

Behind the tip is a fluid lump that is accumulated along the spanwise centre and travels downstream with the vortex loop as identified by the zero relative velocity. The coherent fluid lump is formed as a result of the induced velocity of the vortex loop in the same manner as the displacement thickness is changed. Then the shear layer forms from the faster-moving fluid travelling over the coherent fluid lump.

At the $Z = -1.5$ cm location (figure 17b) a 'flat' region in velocity profiles, $\partial u/\partial Y = 0$, can be observed in the vicinity of the critical layer from phase 30 to 150°. This region corresponds to the core of the vortex-loop leg, which has already been shown to have a negligible ω_Z component, and travels downstream at a constant velocity. As faster-moving fluid flows over the core of the leg, the high-shear layer is formed. It is interesting that, in the spanwise off-centre region, the lower-momentum fluid is contained in the core itself and not transported away from the wall by the vortex loop, as found in the spanwise-centre region of the loop. Thus the momentum-transport concept does not play a direct role in forming this part of the shear layer.

In addition to the region of strong vorticity above the Λ-vortex just described, there exists another region of strong vorticity between the vortex loop and the flat plate (figures 13 and 15). The maxima of ω_Z can be identified in figures 16(a, b) as corresponding to the high-shear layer near the plate. The corresponding ω_X component of vorticity has values as large as those found in the legs of the vortex loop. However, there are significant differences that distinguish these local vorticity maxima from the loop. First, the ω_Z component maxima coincide with the ω_X maxima. The angles

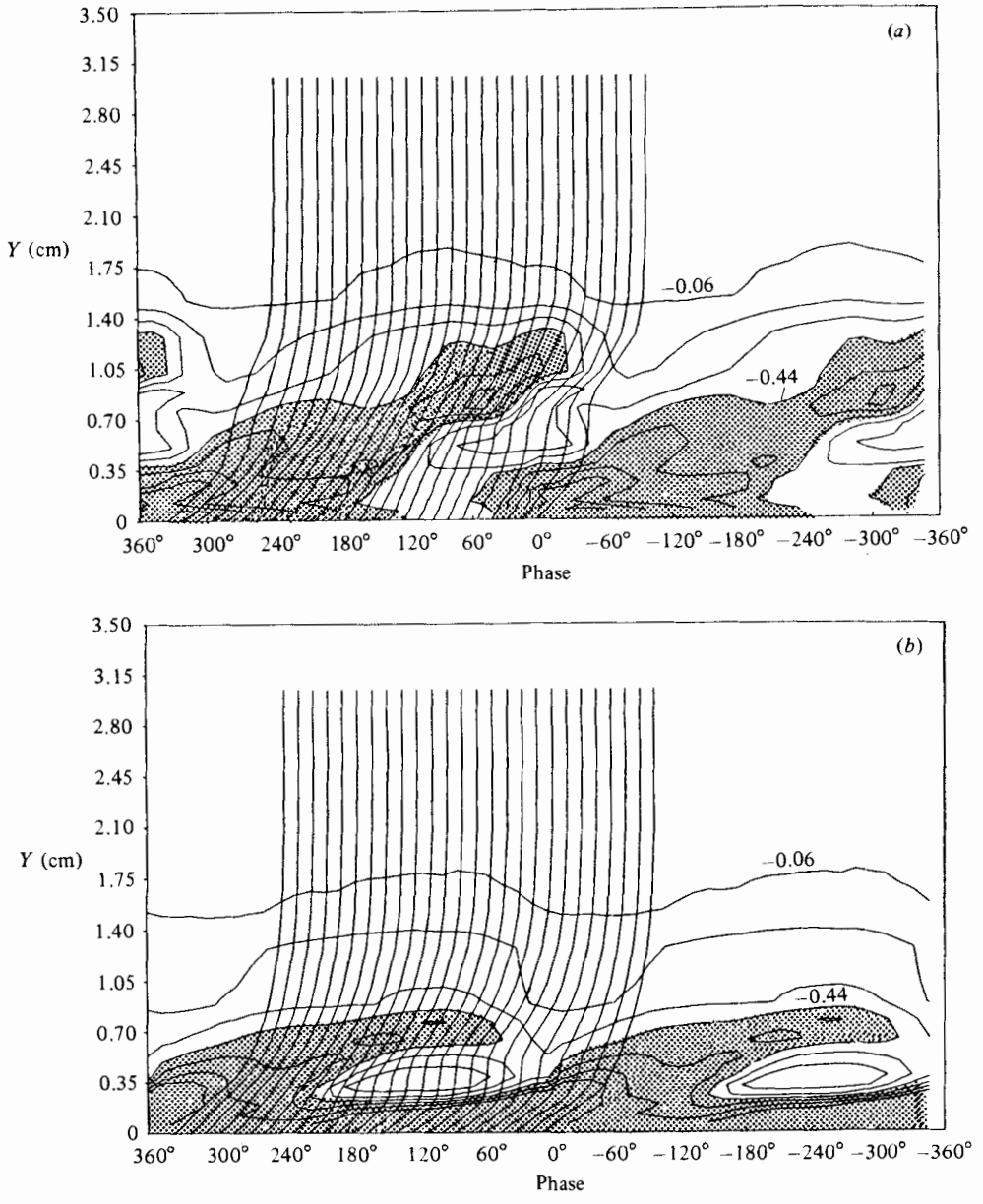

FIGURE 16. Contours of spanwise vorticity superposed with the instantaneous velocity profiles in the (Y, T)-plane at $X = 60$ cm. (*a*) $Z = 0$ cm; (*b*) -1.5 cm. The contours are incremented by $\omega_Z = -0.189$ beginning with $\omega_Z = -0.06$. The shaded regions indicate $\omega_Z \leqslant -0.44$.

of the corresponding vortex lines deviate no more than 15°–19° from the horizontal axis, in contrast with the almost 90° deviation for the legs of the vortex loop. Secondly, the sense of rotation is opposite to that of the vortex loop. Finally, the strong vorticity is spread over a thin layer instead of forming a tube-like structure. Thus this layer of vorticity cannot be the vortex loop observed in flow-visualizaton experiments. Although the layer of vorticity is not inflexional, it may play a role in the later stages of transition (Nishioka, Asai & Iida 1981).

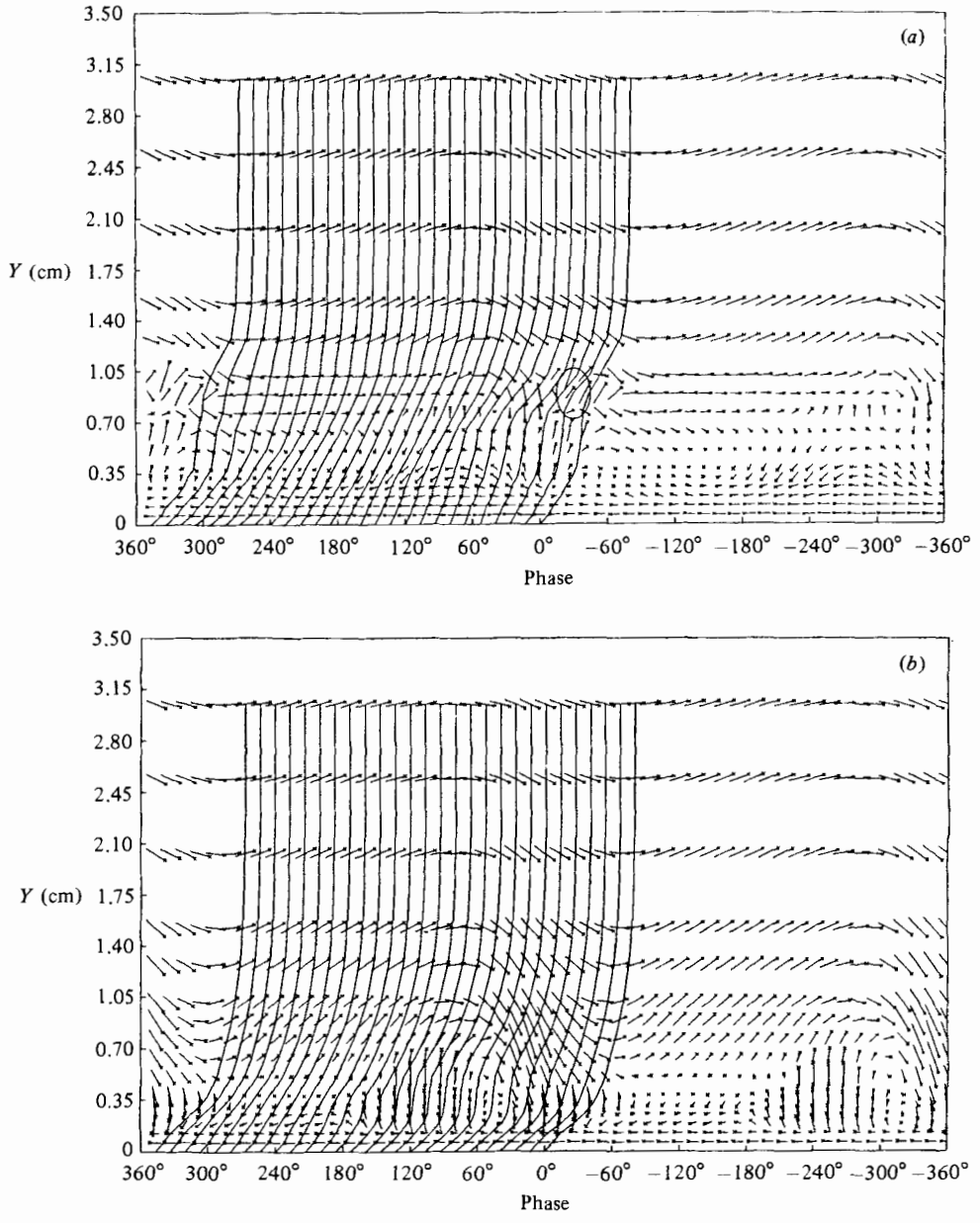

FIGURE 17. Instantaneous velocity profiles in the (Y, T)-plane superposed with the instantaneous projections of the velocity vectors at $X = 60$ cm. (*a*) $Z = 0$ cm; (*b*) -1.5 cm. The circle in (*a*) shows the approximate location of the tip of the vortex loop.

Figure 18 gives a clearer overview of the three-dimensional configuration of the significant vorticity-field structures. The contours of ω_Z vorticity, $\omega_Z = -0.5$, show the high-shear layer, which is above and slightly behind the vortex loop. The loop is mapped out with the contours of $|\omega_X| = 0.13$. (The strong vorticity layer near the wall has been omitted for clarity.) This arrangement of vorticity has escaped earlier detection for two reasons. First, most measurements of vorticity have been limited to that of only $\partial u/\partial Y$, which essentially maps only the high-shear layer. Secondly,

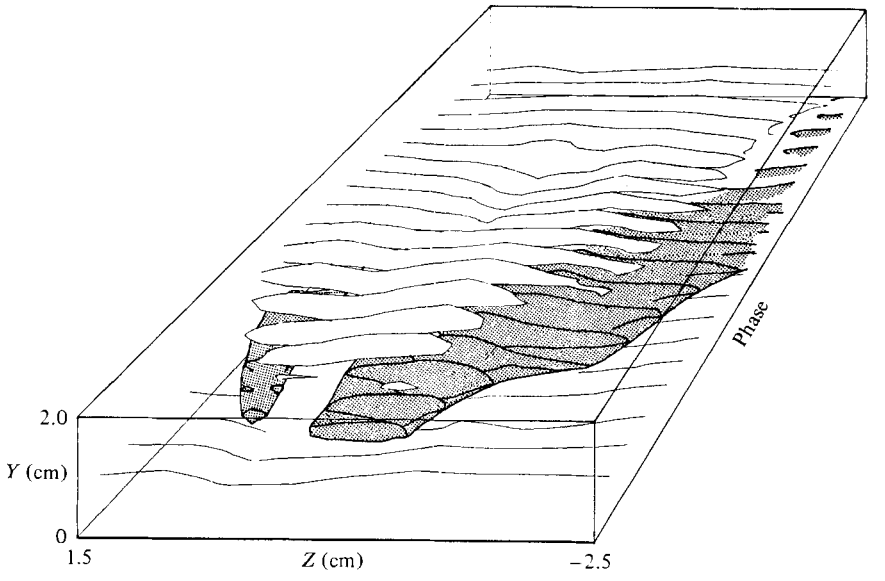

FIGURE 18. Perspective view of the contours of spanwise vorticity ($\omega_Z = -0.5$) and streamwise vorticity ($|\omega_X| = 0.13$), which has been shaded, showing the legs of the vortex loop and the high-shear layer above it. The flow is from the top right to the bottom left side of the page. The region of strong spanwise vorticity near the wall has been omitted for clarity.

it has sometimes been erroneously conjectured that the vortex loop would have the largest magnitude of vorticity in the instantaneous flow field, like a vortex filament. Actually, the total vorticity in the loop has a lower magnitude than that in the high-shear layers, and the transverse component is zero in some regions of the leg. The loop is composed of a core of vortex lines that travel together as the disturbance moves downstream. It is not clear that all three components of velocity must be measured, as in the present investigation, to be able to describe the true nature of the vorticity field and, in particular, to uncover the vortex loop.

6. Conclusions

The instantaneous velocity components in three directions have been measured during the nonlinear, three-dimensional stage of the transition process preceding breakdown by the application of the phase-averaging technique to the hot-film anemometer signals. The mean and instantaneous vorticity fields have been computed from the velocities. The u' phase distributions across the span show the progressive warping of the disturbance wavefront inside the boundary layer as a result of a spanwise variation in phase velocity, in agreement with the vortex loop observed by flow visualization. The vortex loop is shown to exist near the critical layer, and is identified by a strong longitudinal component of vorticity where the transverse vorticity component is minimum. Thus the vortex loop consists of lines of vorticity that are oriented primarily in the streamwise direction. However, in contrast with the earlier idea associated with the visualization studies of the vortex loop, in which the vorticity was thought to be concentrated in the loop, the largest magnitude of instantaneous vorticity actually exists in high-shear layers that are formed above and below, but not in, the vortex loop. The lines of vorticity in these high-shear layers

have primarily a spanwise direction which distinguishes them from the vortex loop. The high-shear layer above the vortex loop is formed by fluid moving faster than the loop, flowing over a coherent lump of fluid in the spanwise centre and over the legs of the loop at off-centre locations. The coherent fluid lump is created by the induced velocity of the vortex loop, and travels downstream with the loop.

In the present study it has been demonstrated that all three components of velocity and vorticity must be determined to fully understand the true three-dimensional nature of the disturbance preceding breakdown. The measurements of $\partial u/\partial Y$ alone cannot detect the presence of the vortex loop, which is primarily composed of ω_X vorticity. On the other hand, the streakline visualization technique marks the centres of the cat's-eye streamline patterns and overemphasizes their behaviour. The cat's-eye flow field is the true structure of a perturbed two-dimensional flow field, and is indeed coherent. It may be conjectured that this coherent body of fluid inside the eyes remains coherent, and only this part of the flow field undergoes the three-dimensional distortion to form the vortex loop. It is then not surprising that the vortex loop does not have the largest vorticity, because, in spite of its appearance, the cat's-eye pattern is associated neither with the vorticity concentration nor even its maxima. In fact, the vorticity fluctuations in the Tollmien–Schlichting waves are minimum near the critical layer, where the centres of the cat's-eye patterns are located.

This investigation was conducted primarily under the support of the Office of Naval Research, U.S. Navy (contract N00014-76-C-0414). The second author (H.F.) actively participated in an early stage of the project during his stay at Princeton University as a Heisenberg Fellow. During the preparation of this paper, D.R.W. was a recipient of the Alexander von Humboldt Research Fellowship.

REFERENCES

Betchov, R. 1960 On the mechanism of turbulent transition. *Phys. Fluids* **3**, 1026.

Bradshaw, P. 1971 *An Introduction to Turbulence and its Measurement*. Pergamon.

Emmons, H. W. 1951 The laminar–turbulent transition in a boundary layer. *J. Aero. Sci.* **18**, 490.

Görtler, H. & Witting, G. 1957 Theorie der sekundären Instabilität der laminaren Grenzschichten. In *Proc. Boundary Layer Research Symp. Freiburg* (ed. H. Görtler), p. 110. Springer.

Greenspan, H. P. & Benney, D. J. 1963 On shear layer instability, breakdown and transition. *J. Fluid Mech.* **15**, 133.

Hama, F. R., Long, J. D. & Hegarty, J. C. 1957 On transition from laminar to turbulent flow. *J. Appl. Phys.* **28**, 388.

Hama, F. R. & Nutant, J. 1963 Detailed flow-field observations in the transition process in a thick boundary layer. In *Proc. 1963 Heat Transfer and Fluid Mechanics Inst.*, p. 77. Stanford University Press.

Hama, F. R., Williams, D. R. & Fasel, H. 1980 Flow field and energy balance according to the spatial linear stability theory for the Blasius boundary layer. In *Laminar–Turbulent Transition* (ed. R. Eppler & H. Fasel), p. 73. Springer.

Klebanoff, P. S., Tidstrom, K. D. & Sargent, L. M. 1962 The three-dimensional nature of boundary-layer instability. *J. Fluid Mech.* **12**, 1.

Kleiser, L. 1982 Numerische Simulationen zum laminar–turbulenten Umschlagsprozess der ebenen Poiseuille-Strömung. Dissertation, Kernforschungszentrum Karlsruhe.

Komoda, H. 1967 Nonlinear development of a disturbance in a laminar boundary layer. *Phys. Fluids Suppl.* **10**, S87.

Kovasznay, L. S. G., Komoda, H. & Vasudeva, B. R. 1962 Detailed flow field in fluid in transition. In *Proc. 1962 Heat Transfer and Fluid Mechanics Inst.*, p. 1. Stanford University Press.

NISHIOKA, M., ASAI, M. & IIDA, S. 1980 An experimental investigation of the secondary instability. In *Laminar–Turbulent Transition* (ed. R. Eppler & H. Fasel), p. 37. Springer.

NISHIOKA, M., ASAI, M. & IIDA, S. 1981 Wall phenomena in the final stage of transition to turbulence. In *Transition and Turbulence* (ed. R. E. Meyer), p. 113. Academic.

ORSZAG, S. A. & KELLS, L. C. 1980 Transition to turbulence in plane Poiseuille and plane Couette flow. *J. Fluid Mech.* **96**, 159.

SCHLICHTING, H. 1933 Zur Entstehung der Turbulenz bei der Plattenströmung. *Nachr. Ges. Wiss., Gött., Math. Phys. Kl.*, p. 182.

SCHLICHTING, H. 1935 Amplitudenverteilung und Energiebilanz der kleinen Störungen bei der Plattenströmung. *Nachr. Ges. Wiss., Gött., Math. Phys. Kl.*, p. 1.

SCHUBAUER, G. B. & SKRAMSTAD, H. K. 1948 Laminar boundary layer oscillations on a flat plate. *NACA Rep.* 909.

STUART, J. T. 1965 The production of intense shear layers by vortex stretching and convection. *AGARD Rep.* 514.

TANI, I. & KOMODA, H. 1962 Boundary layer transition in the presence of streamwise vortices. *J. Aero. Sci.* **29**, 440.

THEODORSEN, T. 1955 The structure of turbulence. *50 Jahre Grenzschichtforschung* (ed. H. Görtler & W. Tollmein), p. 55. Vieweg.

TOLLMIEN, W. 1931 The production of turbulence. *NACA TM* 609.

TOLLMIEN, W. 1936 General instability criterion of laminar velocity distributions. *NACA TM* 792.

WILLIAMS, D. R. 1982 An experimental investigation of the non-linear disturbance development in boundary layer transition. Dissertation, Princeton University.

WORTMANN, F. X. 1977 The incompressible fluid motion downstream of two-dimensional Tollmien–Schlichting waves. *AGARD Conf. Proc.* 224, p. 12–1.

WRAY, A. & HUSSAINI, M. Y. 1980 Numerical experiments in boundary-layer stability. *AIAA Paper* 80-0275.